Chapter 7
Multiscale Modelling of Bionano Interface

Hender Lopez, Erik G. Brandt, Alexander Mirzoev, Dmitry Zhurkin, Alexander Lyubartsev, and Vladimir Lobaskin

Abstract We present a framework for coarse-grained modelling of the interface between foreign nanoparticles (NP) and biological fluids and membranes. Our model includes united-atom presentations of membrane lipids and globular proteins in implicit solvent, which are based on all-atom structures of the corresponding molecules and parameterised using experimental data or atomistic simulation results. The NPs are modelled by homogeneous spheres that interact with the beads of biomolecules via a central force that depends on the NP size. The proposed methodology is used to predict the adsorption energies for human blood plasma proteins on NPs of different sizes as well as the preferred orientation of the molecules upon adsorption. Our approach allows one to rank the proteins by their binding affinity to the NP, which can be used for predicting the composition of the NP-protein corona for the corresponding material. We also show how the model can be used for studying NP interaction with a lipid bilayer membrane and thus can provide a mechanistic insight for modelling NP toxicity.

Keywords Nanoparticle • Toxicity • Coarse-grained molecular dynamics • Protein corona • Cell membrane

7.1 Introduction

Over the last decade, in vitro and in vivo experiments have produced significant amount of veritable information that can be integrated into theoretical models with the aim of predicting possible health and environmental effects of engineered

H. Lopez • V. Lobaskin (✉)
School of Physics, Complex and Adaptive Systems Lab, University College Dublin, Belfield, Dublin 4, Ireland
e-mail: vladimir.lobaskin@ucd.ie

E.G. Brandt • A. Mirzoev • D. Zhurkin • A. Lyubartsev
Department of Materials and Environmental Chemistry, Stockholm University, SE-10691 Stockholm, Sweden

L. Tran et al. (eds.), *Modelling the Toxicity of Nanoparticles*, Advances in Experimental Medicine and Biology, Vol. 947, DOI 10.1007/978-3-319-47754-1_7

nanoparticles (NP) [1]. However, even the most systematic studies leave the question of precise toxicity mechanisms associated with NPs wide open [2–4]. An important finding arising from these studies is that the toxic effects can emerge either from membrane damage or from interaction of NPs, once they are inside the cell, with the internal cell machinery. Therefore, an evaluation of possible risks should include an assessment of NP ability to penetrate, modify, or destroy the cell membrane and bind to key biomolecules [4]. Being selectively permeable, membranes participate in control of the transport of vital substances into and out of cells. Whereas some biomolecules may penetrate or fuse with cell membranes without overt membrane disruption, no synthetic material of comparable size has shown this property [5]. Among the factors determining the outcome of NP-membrane interaction the surface properties of nanomaterials play a critical role, which can implicate the membrane or plasma proteins in conditioning NP prior to cell penetration.

The detailed understanding of the crucial stages of NP-cell membrane interaction can be achieved with computer simulation. Molecular dynamics is now a well-recognized tool for studying intermolecular interactions, self-assembly, and structure of biomolecules or their complexes. The reliability and predictive character of molecular modelling has improved significantly during the last few years, with development of new, carefully parameterized force fields, simulation algorithms, and greatly increased computer power [6]. The role of computer simulation is now well recognized in many fields including drug design and toxicology [7–9]. In the same way, one can attempt to predict the detrimental effect of NPs from physical considerations. Establishing a qualitative and quantitative connection between physicochemical properties of NPs and their effect on biological functioning of membranes can help to identify the possible pathways leading to toxicity and give a mechanistic interpretation of toxicological data. To achieve this goal, one has to understand the processes occurring at the bionano interface or on the initial stages of contact between the foreign nanomaterial and the organism such as formation of NP-biomolecule complexes, NP-cell membrane interaction, and NP uptake into the cell.

Understanding the corona formation and NP uptake requires one to address the lengthscales at the range of up to 100 nanometres, which is currently beyond the reach of direct atomistic modelling. Though lipid membranes have been very intensively studied by molecular simulations during last decade [10], in general, modelling NP translocation through a lipid membrane is a significant challenge. Depending on the size of the NP and any associated proteins (corona) tens of thousands, or more, of lipid and other molecules may be needed to model a representative fraction of the membrane. For small (under 5 nm) NPs, cytotoxicity effects such as membrane disruption and poration can be addressed at the atomistic scale and at this scale significant insights have already been gained using molecular simulation using atomistic or coarse-grained (CG) force fields [11–14]. To assess interactions of larger NPs with membranes mesoscopic simulations based on greatly reduced number of degrees of freedom are required. To build a quantitative mesoscale model, information on NP-biomolecule association should be transferred from atomistic simulations to the larger scale using coarse-graining.

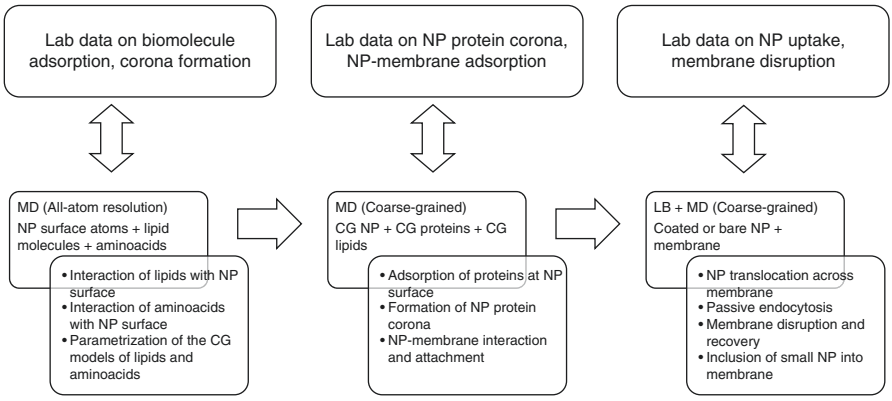

Fig. 7.1 Scheme of the multiscale simulation approach for modelling NP uptake

Many of today's CG models use empirical parameterization of effective interaction potentials. There exist several basic approaches for systematically constructing effective CG potentials from the results of atomistic simulations. One common approach is based on reproduction of forces for specific snapshots of the system (the force matching approach [15, 16] and the other, is based on fitting of structural properties, for which the radial distribution functions are typically used (the inverse Monte Carlo (IMC), or Newton Inversion method) [17, 18]. The IMC method was previously used to build CG models of various molecular systems including ion-DNA solutions [19]. In the same spirit, CG models of plasma and membrane proteins have been developed [20–23] using the united-atom scheme, i.e. replacing the common groups of atoms by single beads, and thus drastically reducing the number of degrees of freedom. The solvent is usually removed from the CG model and is integrated into effective interaction potentials between the CG beads, which on itself provides a big gain in efficiency. A systematic coarse-graining based on the all-atom presentations will preserve the shape and size of the relevant molecules and thus molecular specificity. In this approach we sacrifice a number of internal degrees of freedom, such as protein conformations, which can be justified a posteriori. Although neglecting the protein internal degrees of freedom is a necessarily shaky approximation, this could be the most beneficial one as we can get around the dynamic bottlenecks related to slow protein unfolding.

Similar to molecules, one can use IMC and other coarse-graining methods to model effective interactions between NPs [9, 24, 25]. Thus, the construction of the mesoscale modelling tool involves the following steps, with each consecutive stage based on a systematic coarse-graining of the more detailed description and validated by experimental data (Fig. 7.1):

In the following sections, we describe a minimum set of such CG tools that allow one to simulate the interaction of the NP-protein corona complex with a lipid bilayer. The remainder of the paper is constructed as follows. First, we describe a CG model to calculate the adsorption energies and the most favorable adsorption

orientations of proteins onto a hydrophobic NP. The proposed method is then used to calculate the adsorption energies of the two common proteins in human blood onto NPs with negative or positive surface charge or neutral surface. We also report on the effect of the NP radius on the adsorption energies and validate the proposed methodology against full atomistic simulations. Then, in Sect. 7.3 we describe a methodology, in which full atomistic simulations of a lipid bilayer and various lipid-Cholesterol mixtures are used for the extraction of CG pair potentials. In Sect. 7.4, we present a CG simulation of the interaction a bare NP and of a NP-protein complex with a lipid bilayer. Finally, in Sect. 7.5 we summarise the main results.

7.2 Nanoparticle-Protein Interaction

It is now well accepted that foreign surfaces are modified by the adsorption of biomolecules such as proteins or lipids in a biological environment, and that cellular responses to materials in a biological medium might reflect the adsorbed biomolecule layer, rather than the material itself [26]. Recently, the concept of the NP-protein corona has been introduced to describe the proteins in association with NPs in biological fluids [27–30]. The composition of NP corona is flexible and is determined by many affinity constants and concentrations of the components of the blood plasma. One can speculate that in many practically relevant situations, the protein corona is the surface that is exposed to the cell membrane and is the entity the cell protective mechanisms have to deal with. Thus, for most cases it is more likely that the biologically relevant unit is not the particle itself, but a nanoobject of specified size, shape, and with certain protein corona structure. Naked particle surfaces will have a much greater (non-specific) affinity for the cell surface than a particle hiding behind a corona of "bystander" proteins – that is proteins for which no suitable cellular recognition machinery exists. The evidence suggests that, in comparison to typical cell-membrane-biology event timescales, the particle corona is likely to be a defining property of the particle in its interactions with the cell surface, whether it activates cellular machinery or not. Similar observations and outcomes exist for particles inside the cell, in key locations, though we cannot discuss details here [27–30]. We assume that the actual content of the corona is determined by (i) the NP exposure to the protein solution (blood plasma), (ii) a competition between the adsorbed proteins and the glycoproteins/membrane lipids. We will model the protein and lipid interaction with the NP surface at the CG united-atom level for selected set of proteins (see Table 7.1) and lipids. These simulations will provide interaction energies and will be used to predict the kinetics of protein/lipid corona formation. The data on aminoacid interaction with NP will allow us to compute binding affinities of arbitrary proteins of known structure within an additive model implying that the total protein-NP interaction energy is computed as a sum of NP interactions with aminoacids in contact with NP surface. From the typical protein concentrations and adsorption energies one can also predict the average content of the corona using ideal adsorbed solution theory [31]. It is important to understand

Table 7.1 Proteins, PDB ID used for the coarse-graining and the abbreviations used in the text, and their size and abundance in human blood plasma

Protein	PDB ID	Abbreviation	Weight fraction in plasma, %	Molar mass in, kDa
Human Serum Albumin	1N5U	HSA	5.0	67
Fibrinogen	3GHG	Fib	0.4	340

that at this stage we would be able neither to scan all the plasma proteins nor to take into account any change of protein conformation or bonding between the adsorbed proteins. However, as the effect of the corona is still largely unknown, we can only hope to capture the most important contributions of the plasma protein to the NP dispersion stability and their interaction with the cell membrane.

Due to complexity of blood plasma, we can only model it at a simplified level. It seems reasonable to include the elements, which are more likely to affect the NP interactions and aggregation, and mediate their interaction with the membrane. The plasma can then be modelled as a solution of biomolecules in an implicit solvent with a dielectric constant of water and the Debye length corresponding to physiological ionic strength, van der Waals interactions set to corresponding triplets NP-protein-water, or protein-water-protein, and appropriate surface charges on the molecules. In this work, we study the adsorption of two of the most abundant proteins in blood plasma, Human Serum Albumin (HSA) and Fibrinogen (Fib). In Table 7.1, we summarise their relative content in blood and their molar mass. Although this two proteins represent important components of the blood plasma because of their abundance, recent observations [27–29, 32] demonstrate that the protein corona can include hundreds of different plasma proteins. As of now, it is mostly not known what proteins dominate the content of the corona or play the most crucial role in the NP coating and uptake, although some progress has been made [33] and there is hope that such information will become available in the coming years.

7.2.1 Adsorption of Proteins onto Nanoparticles

The starting point for development of a CG model for the interaction of NPs with proteins is to decide how much detail from the molecular structure of the protein one needs to keep. There is an active and extensive research activity on the different CG models that can be used to simulate proteins under different conditions (for more detailed reviews see [20, 22, 34]). The aim of this work is to propose a set of tools that could be used to simulate the interaction of one or more proteins (and in some cases quite big proteins) with a NP, for relatively long timescales. To meet this goal with a reasonable computational effort the number of beads representing the protein should be kept as small as possible but the proposed model should also preserve enough structural information about the molecule. For these reasons we

Table 7.2 Normalized hydrophobicities ε_i (taken from Table II in [21]) and σ_i for each amino acid (taken from [38])

Residue	LYS	GYU	ASP	ASN	SER	ARG	GLU	PRO	THR	GLY
ε_i, ε	0.00	0.05	0.06	0.10	0.11	0.13	0.13	0.14	0.16	0.17
σ_i, nm	0.64	0.59	0.56	0.57	0.52	0.66	0.60	0.56	0.56	0.45
Residue	HIS	ALA	TYR	CYS	TRP	VAL	MET	ILE	PHE	LEU
ε_i, ε	0.25	0.26	0.49	0.54	0.64	0.65	0.67	0.84	0.97	1.00
σ_i, nm	0.61	0.50	0.65	0.55	0.68	0.59	0.62	0.62	0.64	0.62

The most hydrophilic residue has a ε_i of 0, while the most hydrophobic has a value of 1. For residue-residue interactions, we use the Lorentz-Berthelot mixing rules $\sigma_{i,j} = \left(\sigma_i + \sigma_j\right)/2$, $\varepsilon_{i,j} = \sqrt{\varepsilon_i \varepsilon_j}$

propose a one-bead-per-residue model and consider the structure of the protein as a rigid body. We have studied the predictions of this model in more detail in Ref. [35]. The crystal structures of the proteins are obtained from the literature and one bead is per amino-acid is placed at the position of the α-carbon. At the end of this section, we will test the validity of this first approximation. The second approximation is what level of detail will be needed to represent the NP. In this work, we will consider spherical homogeneous NPs so a single-bead representation is justified.

In our model, the total NP surface-protein interaction potential (U) is a function of distance from the surface to the centre of mass (COM) of the protein, d_{COM} and of protein orientation. It is given by a sum of two contributions:

$$U = \sum_{i=1}^{N} \left(U_i^{\mathrm{VdW}} + U_i^{\mathrm{el}} \right) \tag{7.1}$$

where N is the total number of residues in the protein, U_i^{VdW} is the van der Waals interaction of residue i with the surface and U_i^{el} is the electrostatics interaction of residue i with the surface.

For van der Waals contribution to the potential energy we propose a modified version of the residue-residue interaction potential as suggested in [21]. The model is based on the widely used residue-residue interaction energies proposed by Miyazawa and Jernigan [36], but instead of having a 20×20 interaction matrix this is reduced to a table of normalized hydrophobicities, ε_i, one for each amino acid (see Table 7.2 in [21]). A hydrophobicity index 0 is assigned to the most hydrophilic residue (LYS) and an index 1 to the most hydrophobic one (LEU). We should stress that any other hydrophobicity scale can also be used, it just has to be transformed such that the indices have to be between 0 and 1, where 0 is assigned to the most hydrophilic residue while 1 to the most hydrophobic one. In this work, we consider a generic surface which chemical reactivity that can be modeled as another residue with a hydrophobicity index ε_s.

To model interaction of biomolecules with particles of different sizes we use the following model for the nanomaterial. We assume that the interaction between a residue *i* and a bead of the NP *s* being at a distance *r* from each other is given by a modified 12-6 Lennard-Jones potential:

$$U_{s,i}(r)=\begin{cases}4\varepsilon_{e,n}\left[\left(\frac{\sigma_{s,i}}{r}\right)^{12}-\left(\frac{\sigma_{s,i}}{r}\right)^{6}\right]+\varepsilon_{e,n}\left(1-\varepsilon_{s,i}\right) & r<r_{c,i}\\ 4\varepsilon_{e,n}\varepsilon_{s,i}\left[\left(\frac{\sigma_{s,i}}{r}\right)^{12}-\left(\frac{\sigma_{s,i}}{r}\right)^{6}\right] & r_{c,i}\le r\le r_{\text{cut}}\\ 0 & r>r_{\text{cut}}\end{cases} \tag{7.2}$$

$\varepsilon_{e,n}$ is a parameter that scales the interaction energy, $\varepsilon_{s,i}$ is the combined hydrophobicity index of residue *i* and the nanomaterial and is given by $\varepsilon_{i,s}=\sqrt{\varepsilon_i\,\varepsilon_s}$, $\sigma_{s,i}$ is the average van der Waals radius of residue *i* and the nanomaterial bead, $\sigma_{s,i}=(\sigma_s+\sigma_i)/2$, $r_{c,i}$ is the position of the minimum of the pair potential.

An integration of the 12-6 potential over the volume of the nanomaterial as defined in [21] gives a 9-3 Lennard-Jones-type potential. For a flat surface, the interaction can be expressed in terms of *d,* the distance between the residue centre of mass the closest element of the surface. An integration over a semi-space gives:

$$U_{si}^{\text{vdW}}(d)=\begin{cases}\varepsilon_{es}\rho\sigma_{s,i}^{3}\left[\left(\frac{\sigma_{s,i}}{d}\right)^{9}-\frac{15}{2}\left(\frac{\sigma_{s,i}}{d}\right)^{3}+\left(\frac{125}{2}\right)^{\frac{1}{2}}\left(1-\varepsilon_{s,i}\right)\right] & d<d_{c,i}\\ \varepsilon_{es}\varepsilon_{s,i}\rho\sigma_{s,i}^{3}\left[\left(\frac{\sigma_{s,i}}{d}\right)^{9}-\frac{15}{2}\left(\frac{\sigma_{s,i}}{d}\right)^{3}\right] & d_{c,i}\le d\le d_{\text{cut}}\\ 0 & d>d_{\text{cut}}\end{cases} \tag{7.3}$$

where $\varepsilon_{es}=4\pi/45\,\varepsilon_{e,n}$, ρ is the number density of beads in the nanomaterial, *d* is the distance from the residue *i* to the surface, $d_{c,i}=(2/5)^{1/6}\sigma_{s,i}$. Although the density ρ seems to be an important parameter scaling the interaction, it is not independent and therefore is not crucial for our method. From fitting the adsorption energy to experimental or MD simulation data, we can find the composite quantity $\varepsilon_{es}\rho$, which is

sufficient for further calculations. For a NP of radius R, a similar integration over the particle volume gives:

$$U_{si}^{\mathrm{vdW}}(r)=\begin{cases}4\varepsilon_{es}\rho\sigma_{s,i}^{3}\left[\dfrac{\left(15r^{6}R^{3}+63r^{4}R^{5}+45r^{2}R^{7}+5R^{9}\right)\sigma_{s,i}^{9}}{\left(r^{2}-R^{2}\right)^{9}}-\dfrac{15R^{3}\sigma_{s,i}^{3}}{\left(r^{2}-R^{2}\right)^{3}}\right]-U_{c}^{\mathrm{vdW}}\left(1-\varepsilon_{s,i}\right) & r<r_{c,i}\\ 4\varepsilon_{es}\,\varepsilon_{s,i}\rho\sigma_{s,i}^{3}\left[\dfrac{\left(15r^{6}R^{3}+63r^{4}R^{5}+45r^{2}R^{7}+5R^{9}\right)\sigma_{s,i}^{9}}{\left(r^{2}-R^{2}\right)^{9}}-\dfrac{15R^{3}\sigma_{s,i}^{3}}{\left(r^{2}-R^{2}\right)^{3}}\right] & r_{c,i}\le r\le r_{\mathrm{cut}}\\ 0 & r>r_{\mathrm{cut}}\end{cases} \tag{7.4}$$

where r is the distance from residue i to the centre of the NP. The distance $r_{c,i}$ corresponds to the minimum of the potential and U_c^{vdW} is the value of the function $U_{s,i}^{\mathrm{vdW}}(r_{c,i})$ as defined in the range $r_{c,i}\le r\le r_{\mathrm{cut}}$. We do not show the general expression for the position of the minimum as it is too bulky. The minimum is located at $r_{c,i}-R\approx(2/5)^{1/6}\,\sigma_{s,i}$ at $R\gg\sigma_{s,i}$ and is displaced to shorter distances at smaller R. The variation, however, is not very large, at $R\to\infty$, $r_{c,i}-R\approx 0.858374\sigma_{s,i}$, at $R=200\sigma_{s,i}$ it is $0.858375\sigma_{s,i}$, at $R=20\sigma_{s,i}$ it is $0.858469\sigma_{s,i}$, at $R=2\sigma_{s,i}$ it is $0.865242\sigma_{s,i}$.

Note that the potential in Eq. (7.2) will only give a repulsive interaction between a highly hydrophilic surface and any residue (*i.e.* defining $\varepsilon_s=0$, gives $\varepsilon_{s,i}=0$ for all residues). On the other hand, assigning a non-zero value for ε_s will only change the magnitude of the interaction between any residue and the surface but not the shape of the potential. In this way, the proposed potential is limited to model only hydrophobic surfaces. Because of this limitation, we set the value of $\varepsilon_s=1$ for all simulations. Alternatively, a potential that includes desolvatation penalties, as the 12-10-6 Lennard-Jones potential proposed in [37, 38] for residue-residue interactions or the modified version proposed in [23] used to model residue-surface interactions, can be used to generate a more general interaction potential. The main drawback of the use of these more refine formulas for the potential is that the parameterization is more challenging, and the applicability of a set of parameters could be very narrow.

The electrostatic interactions in Eq. (7.1) is modeled by adding point charges on the NP surface. This charges interact with the charged residues via a Debye-Hückel potential. The electrostatic interaction energy between a residue i and all the charges on the surface is given by:

$$U_i^{\mathrm{el}}=\sum_{j}^{N_p}\lambda_B k_B T q_i q_j\,\frac{\exp\left(-r_{ij}/\lambda D\right)}{r_{ij}} \tag{7.5}$$

where r_{ij} is the distance between the residue i and the point charge on the surface j, $\lambda_B=e^2/(4\pi\varepsilon_0\varepsilon_r k_B T)$ is the Bjerrum length, k_B is the Boltzmann constant, T the

temperature, ε_0 the dielectric permittivity of vacuum, ε_r the relative dielectric permittivity of water, q_i the charge of residue *i*, q_j the charge of the point charge *j* on the surface, N_e the total number of point charges on the surface and λ_D is the Debye length (defined through $\lambda_D^{-2} = 8\pi\lambda_B c_0$, with c_0 is the background electrolyte concentration). In practice, the points charges are evenly distributed on the spherical surface of the NP using a Golden Section spiral algorithm and all points will have the same charge q_j given by $q_j = 4\pi\sigma R^2/N_e$, where σ is the surface charge density of the NP and R is the radius of the NP.

7.2.2 *Orientational Sampling and the Calculation of the Adsorption Energy*

In this work, we are not considering conformational changes during the adsorption process and assume that proteins are rigid. Although the adsorption process might conduce to conformational changes, this events happen at longer times than orientational changes on the surface [39]. Taking this into account, the adsorption energies calculated here will give a valuable insight into the long-time evolution of the of the NP-protein corona content.

In our CG model, each residue of a protein is represented by a single bead located at the α-carbon position. The native structures are obtained from the Protein Data Bank, and in Table 7.1 we report the proteins studied in this work, the PDB ID from which the CG model were built and the abbreviation that will be used in the rest of the text. The chosen proteins are some of the most abundant in human blood and will have a major influence in the formation of the NP protein-corona.

To identify the most favourable orientation of adsorbed protein globule (the one with the minimum adsorption enthalpy) we will follow the method suggested in [40], which is not as efficient as *e.g.* a genetic algorithm, but can provide additional information about the adsorption process. Briefly, a configuration space search is performed, where a systematic rotation of the protein allows us to build an adsorption map. There are three degrees of freedom (DOF) that have to be scanned. Figure 7.2 shows that any point on the surface of the protein can be defined by a position vector from the COM of the protein. This vector is characterised by two angles: ϕ and θ and by rotating the molecule an angle $-\phi$ around the z direction and then by an angle $-\theta + 180°$ around the y axes will make the position vector point towards the surface. The third DOF is the distance from the COM to the closest point of the surface, d_{COM}. Here, we sample ϕ from 0 to 350° in steps of 10° and θ from 0 to 170° in steps of 10° (note that $\phi = 0°$ is equivalent to $\phi = 360°$, and that $\theta = 0°$ is equivalent to $\theta = 180°$). Instead of obtaining the "real" adsorption free energy by calculating the potential of mean force for all orientations, we only calculate the potential energy U (given by Eq. (7.1)), which is the sum of all the interactions between the surface and the protein. As the adsorption energies are expected to be at least five times $k_B T$ and as the proteins are assumed to be rigid, neglecting thermal fluctuations

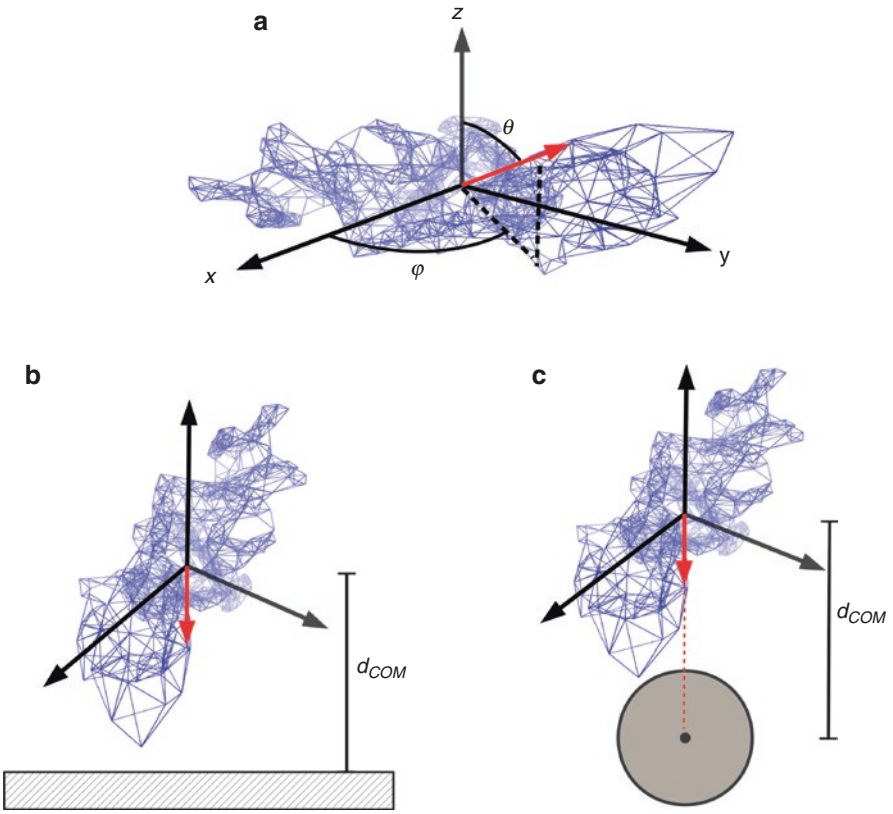

Fig. 7.2 Definition of the protein orientation. (**a**): Any point on the surface of the protein can be defined by a position vector from the COM to that point and depends on two angles ϕ and θ. The remaining degree of freedom is the distance of the COM, d_{COM} to (**b**) the surface for a slab or (**c**) to the center of the NP

is clearly justified. For each configuration (ϕ_i, θ_j), the total potential energy is calculated as a function of distance of the COM, U (d_{COM}, ϕ_i, θ_j), to the surface for the case of a slab (Fig. 7.2b) or to the center of the NP for the case of a NP (Fig. 7.2c). Following a similar approach as in [41], and denoting the reaction coordinate $d_{COM} = z$, the adsorption energy for any particular configuration in the case of a protein adsorbing on a flat surface is given by:

$$E\left(\phi_i,\theta_j\right) = -k_B T \ln\left[\frac{1}{a\left(\phi_i,\theta_j\right)}\int_0^{a\left(\phi_i,\theta_j\right)} \exp\left(-U\left(\phi_i,\theta_j,z\right)/k_B T\right) dz\right] \tag{7.6}$$

where $a(\phi_i, \theta_j)$ is the maximum interaction distance from the COM of the protein to the surface for the given orientation. For the case of a NP-protein interaction, the mean interaction energy for any particular orientation is given by:

$$E\left(\phi_i,\theta_j\right) = -k_B T \times \ln\left[\frac{3}{\left(R + a\left(\phi_i,\theta_j\right)\right)^3 - R^3}\int_R^{R+a\left(\phi_i,\theta_j\right)} z^2 \exp\left(\frac{-U\left(z,\phi_i,\theta_j\right)}{k_B T}\right) dz\right] \tag{7.7}$$

Then the total mean adsorption energy of the system for both cases (slab and NP), E_{ad}, can be estimated by averaging over all adsorbed states with Boltzmann weighting [40]:

$$E_{ad} = \frac{\sum_i \sum_j P_{ij} E\left(\phi_i,\theta_j\right)}{\sum_i \sum_j P_{ij}} \tag{7.8}$$

where $P_{ij} = \sin(\theta_j) \exp[-E(\phi_i, \theta_j)/k_B T]$ is the Boltzmann weighting factor.

7.2.3 Details of the Simulations, Parameterisation and Validation

All simulation were performed using ESPResSo MD package [42] and the cutoff for the interaction potential in Eq. (7.2) was set to $r_{cut} = 6$ nm. For all calculations the simulation box was taken big enough to fit the NP and the protein. The method described here only involves the calculation of the total energy of the system given by Eq. 7.1, therefore a coupling to a thermostat is not required. After the CG model were built from the PDB files, the obtained structures were shifted so the COM of the molecules was in the origin of the frame of reference and this structure was defined as the ($\phi = 0°, \theta = 0°$) orientation. With this definition the first residue in the sequence of each protein will have the following (ϕ, θ) angles: (21.4°, 85.2°) for HSA and (132.1°, 46.4°) for Fib.

The units of the simulations are: lengths (L) in nm, energy (ε) in $k_B T \approx 4.15 \times 10^{-21}$ J taking a temperature of $T = 300$ K, for the mass unit (M) we selected the average mass of the 20 residues (ca. 110 Da) hence in our simulations all residues have a mass of 1. The values of ε_i and σ_i can be found in Table 7.2 and as mentioned in Sect. 7.2.1 we will only consider hydrophobic NPs with $\varepsilon_s = 1$ and $\sigma_s = 0.35$ nm.

NPs with negative surface charges as well as neutral NPs were considered. For the negatively charged ones, a surface charge density of -0.02 C/m^2 was used. As explained in Sect. 7.2.1, the charged surfaces are modelled by individual point charges. The surface density of these charged beads ($\sigma_c = N_e/R^2$) was set to 4 nm^{-2} for all the simulations, which gives e.g. a $N_e = 100$ for a NP of $R = 5$ nm. Then, we

assumed that each bead carries a charge of $-0.39e$, where e is the elementary charge. As we are considering physiological conditions, we use $\lambda_B = 0.73$ nm and $\lambda_D = 1$ nm. Residue charges at this condition are $+e$ for LYS and ARG, $-e$ for ASP and GLU, and $+0.5e$ for HIS. The rest of the residues are neutral.

The only free parameters of the model are $\rho\varepsilon_{es}$ in Eq. (7.2), and the parameterisation was done by systematically changing its value to match experimental data of adsorption of Lysozyme on hydrophobic surfaces reported by Chen et al. [43]. The native structure for our CG model of Lysozyme was obtained from the PDB ID: 2LYZ. With $\rho\varepsilon_{es} = 1.972 k_B T/\text{nm}^3$ we obtain a value of $-7.6 k_B T$ for the adsorption energy (very close to the experimental reported value of $-7.9 k_B T$).

To validate the parameterization, the adsorption energy of Myoglobin (PDB ID: 1MBN used for the CG model) was calculated using the same value of $\rho\varepsilon_{es}$ obtained from the parameterisation. In this way, a value of $-6.1 k_B T$ was found for the adsorption energy of Myoglobin. This value is slightly lower that the experimental value of $-7.6 k_B T$ also reported by Chen et al. [43] but reproduces the trend that Myoglobin adsorbs slightly weaker than Lysozyme to a hydrophobic surface.

7.2.4 Protein Adsorption Energies

Results for the adsorption energies calculated using Eq. (7.8) as a function of NP radius are shown in Fig. 7.3. The results show that HSA adsorbs stronger as the radius of the NP increases until the energy reaches a minimum value (Fig. 7.3a). For small NPs, the combination of the size effect (increasing R increases the van der Waals interactions) with the availability of residues to interact with the surface ensures that the proteins adsorb stronger (more negative values) as the radius is increased. Then, after a value of radius around 50 nm, the E_{ad} starts to converge to the value corresponding to a flat surface as the van der Waals interactions and the number of residues close to surfaces do not change significantly by increasing R. We performed calculations for NPs of R up to 500 nm and confirmed that the adsorption energy indeed converges to the slab values. For the Fib molecule the situation is different (Fig. 7.3b). In this case the adsorption energy decreases as a function of R at least until the biggest radius studied here (R = 100 nm) and it is lower than for the adsorption onto a flat surface. The big size of the Fib molecule (ca. 45 nm on its longest axes) makes that for at least until R = 100 nm the combined effects of curvature and number of residues that interact with the surface are still noticeable. The effect of the charge is more important for the HSA that for the Fib. HSA charge is overall negative, so the electrostatic interactions contribution is mainly repulsive increasing the values of the E_{ad}. On the other hand, the Fib molecule's charge is positive and the electrostatic interactions tend to increase the adsorption of the Fib onto a negative surface. In neither of the proteins the maximum contribution of electrostatic interactions was more than $3 k_B T$.

The systematic sampling employed for the calculation of the adsorption energies can also be used to identify the most favourable orientations for adsorption and to

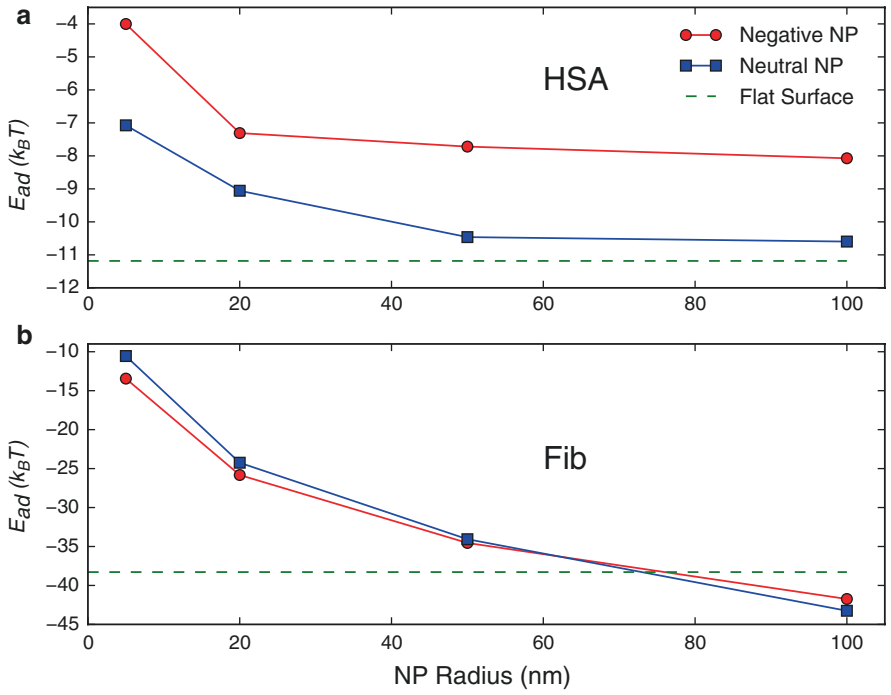

Fig. 7.3 Adsorption energies as a function of the NP radius for the proteins studied and the two types of surface charge: Negative: -0.02 C/m^2 and Neutral: no charge. Subfigure (**a**) shows the results for HSA and (**b**) for Fib. The dashed lines show the adsorption energy for the case of a flat surface

study how the charge and/or the radius of the NP influence the protein orientation. Figure 7.4 shows a surface map of the adsorption energy as a function of the angles θ and ϕ for HSA. Each panel is for a radius of 5 or 100 nm and for a neutral or a negatively charged surface. The surfaces are complex in structure showing an energy landscape with several local minima with differences less than $1k_BT$. It is also important to notice that the maps have large areas with adsorption energies of $-6k_BT$ or lower. Our results show that HSA will strongly adsorb at physiological conditions and room temperature and that orientational changes after adsorption are energetically favourable. Comparison of different panels in Fig. 7.4 shows that radius has only a small effect on the preferred orientations, while the NP surface charge density has a minor impact on the preferred orientations.

A different scenario is observed for Fib. Figure 7.5 shows colour maps of Fib adsorption energy for two radii for neutral and charged surfaces. In this case, the maps depend on the radius of the NP (compare Fig. 7.5a with Fig. 7.5b or Fig. 7.5c with Fig. 7.5d) but change very little between the charged and uncharged surface (compare Fig. 7.5a with Fig. 7.5c or Fig. 7.5b with Fig. 7.5d). As we already noticed for HSA, the charge has a small effect on the total adsorption energy so we do not expect that it

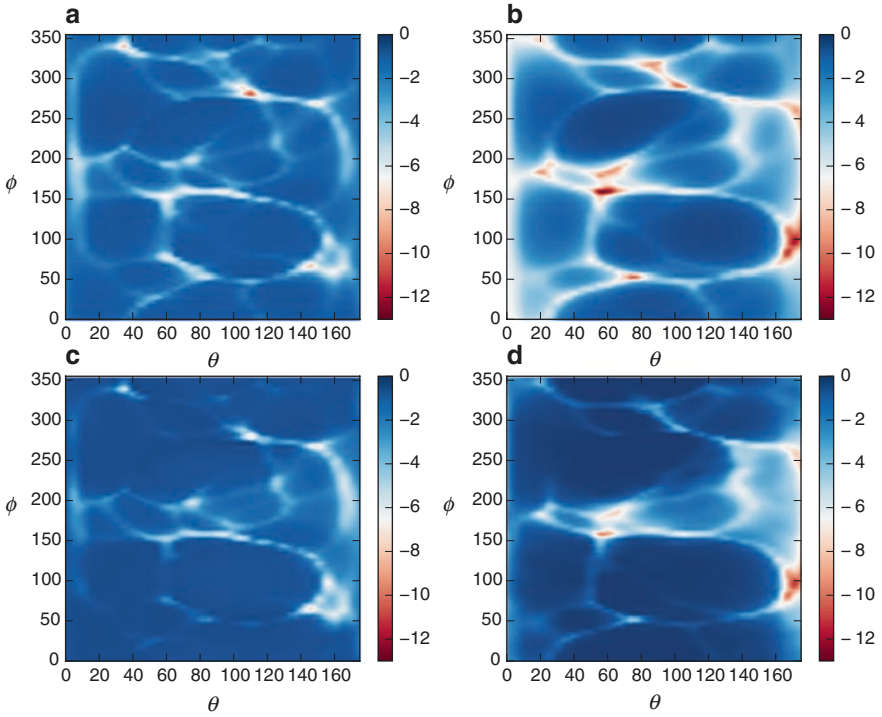

Fig. 7.4 Adsorption energy maps for HSA. (**a**) Neutral particle of $R = 5$ nm. (**b**) Neutral particle of $R = 100$ nm. (**c**) Negatively charged particle of $R = 5$ nm. (**d**) Negatively charged particle of $R = 100$ nm

would dramatically change the energy maps. The radius and the surface curvature seem to be more important as for big proteins (like Fib) a larger NP allows a more extensive contact and thus influences the preference for protein orientations (or NP binding pockets). In Fig. 7.6, we show the most favorable orientations for Fib on a neutral surface for two different NP radii. For the small NP (Fig. 7.6a), Fib has its adsorption energy minimum in a configuration where the NP interacts with a relatively small segment of the molecule. Meanwhile, for a large NP, Fib tends to bind in a completely different orientation (Fig. 7.6b). Now the most favourable orientation is the one with the longest axis of the Fib molecule along the surface.

A straightforward conclusion from the above data is that the bigger the protein, the stronger it will bind to a NP. This result agrees with the experimental observation reported by De Paoli et al. [44], which shows that the binding association constant on citrate-coated gold NPs (which can be considered as moderately negative hydrophobic NP) depends mainly on the size of the protein (they studied HSA, Fib and other blood proteins). It is interesting also to compare our results with the simulations of NP corona formation reported by Vilaseca et al. [45]. Using CG MD simulations, they found that for a flat surface at long times the most abundant protein adsorbed was Fib, then Immunoglobulin-γ (of intermediate size between HSA and

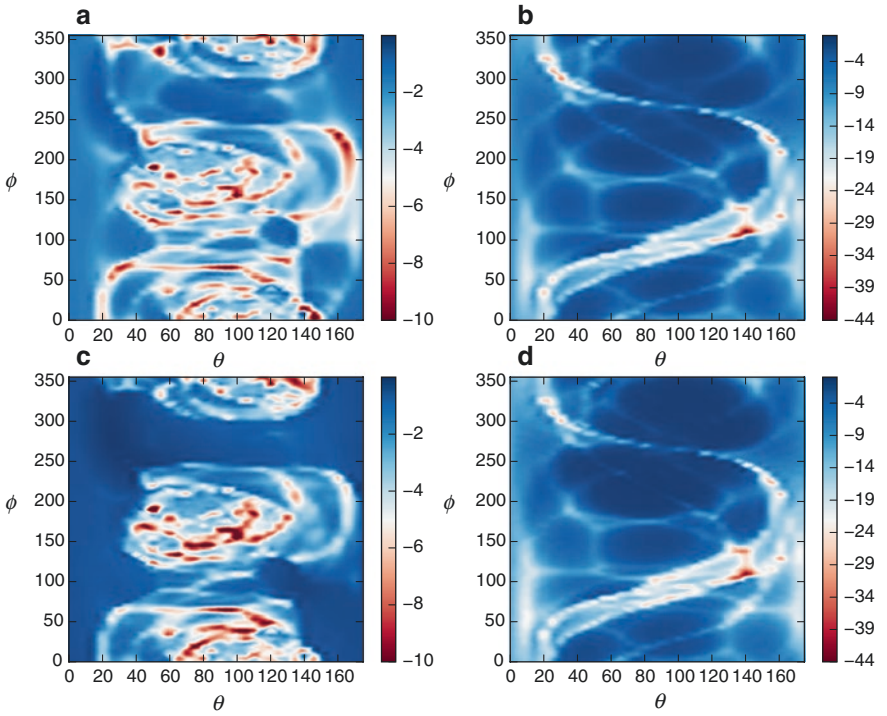

Fig. 7.5 Adsorption energy maps for Fib. (**a**) Neutral surface and $R = 5$ nm. (**b**) Neutral surface and $R = 100$ nm. (**c**) Negatively charged surface and $R = 5$ nm. (**d**) Positively charged surface and $R = 100$ nm

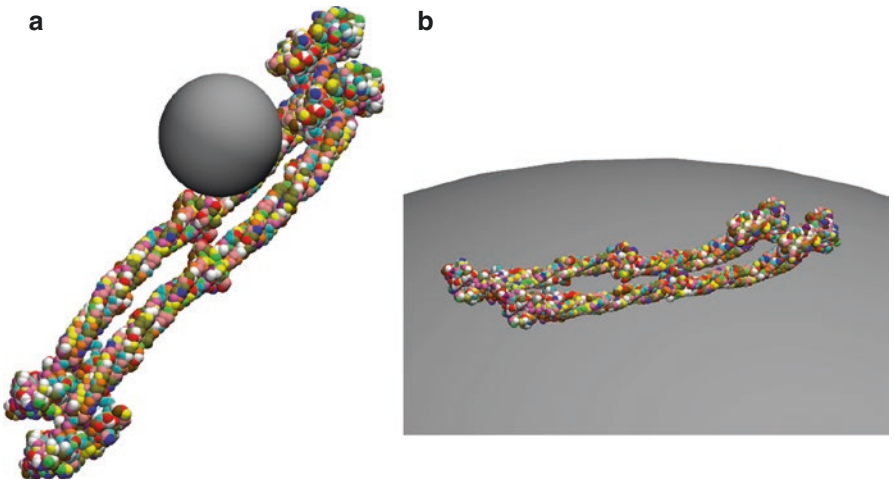

Fig. 7.6 Fib most favorable orientation for adsorption on a neutral surface: (**a**) $R = 5$ nm and (**b**) $R = 100$ nm

Fib) and at last HSA. We should note that the adsorption energies calculated in this work will be a good predictor of the equilibrium composition of the NP-protein corona while at short times other factors such as the protein sizes and their concentrations have to be considered to predict the corona composition.

We should note that the approach presented here is justified for small NPs but may be difficult to use with large NPs for two main reasons. First of all, the interaction potential resulting from integration of the van der Waals forces over the volume of the NP will become long-range in that case. Here, we explicitly assumed that the particle is hydrophobic, so that there a non-negligible attraction will be felt by the protein far away from the NP (up to tens of nanometers), well beyond the typical range of the interactions of individual molecules. In our example, the prefactor $\varepsilon_{s,i}$ scales the interactions, so that the attraction is strongest between the hydrophobic NP and the hydrophobic residues. We performed the energy calculation without any cut-off but had to limit the interaction radius in the MD simulation below to 6 nm. Second, it is not a priori clear whether the same hydrophobicity coefficient $\varepsilon_{s,i}$ can be used to describe the interaction of the bulk material of the NP with the protein as we determined for the surface beads. While the interaction at small distances is modified by water structuring at the surface, the long-range van der Waals force should not be affected by the local effects. Therefore, the coefficients for hydrophilic materials may underestimate the attraction between the NP and biomolecules. To overcome this limitation, one needs to treat the bulk of the NP differently from the surface layer. From this point of view, it would be reasonable to introduce a two-layer model of a NP, where the surface layer takes into account hydration and the attraction of biomolecules to the NP is not underestimated due to the short cut-off. To include the attraction in full, one must use cut-off distances of at least particle diameter, i.e. 5 nm for 2.5 nm NP, 10 nm for 5 nm NP, etc. The main issue to be solved in future modelling is how to increase the cut-off of the NP bulk material interaction with the biomolecule beads in common simulation codes without affecting dramatically the computational cost.

7.2.5 Validation of the Methodology

We now test our CG methodology with predictions of full-atomistic MD simulation. We model adsorption of small plasma protein Ubiquitin (Ubi) to a flat TiO_2 surface. The reasons for choosing Ubi for the validation was due to the its small size (only 76 residues) and known folded structure, which allows us to perform full atomistic simulations in a reasonable amount of time.

The Ubi crystal structure was obtained from the PDB (PDB ID file 1Ubi [46]) and was coarse-grained as explained above (see Fig. 7.7). To be able to directly compare against full atomistic simulations, in this case the interactions potentials between the 20 different residues and the surface were obtained by performing full atomistic simulations of the adsorption of each of the 20 aminoacids and then performing an inverse Monte Carlo calculation.

Fig. 7.7 CG model of Ubi (PDB ID: 1Ubi [46]). In our model each residue in the protein is represented by one bead

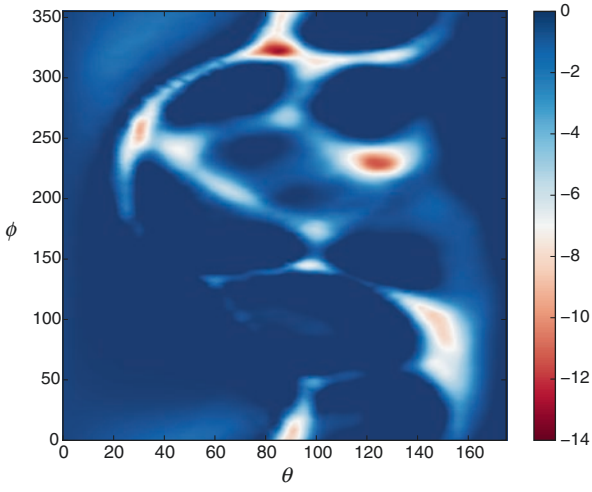

Fig. 7.8 Adsorption energy maps for Ubi adsorbing into a TiO_2 slab

With the CG methodology we obtained the total adsorption energy of $-10.7k_BT$ for Ubi and the adsorption map is shown in Fig. 7.8. The surface obtained shows two major minima and a number of local minima. It also predicts that orientational changes are favorable after adsorption as some of the minima are connected by an energy landscapes with rather small barriers (less than $3k_BT$).

To analyse the validity of our model and to understand the dynamical behavior of the adsorption process we performed a series of full atomistic simulations. We used the VESTA program [47] to construct a 5 × 20 × 32-supercell of the TiO_2 rutile unit cell. The coordinates were rotated so that the normal of the TiO_2 slab, corresponding to the (100) surface, was oriented along the z-direction. The box was elongated in the z-direction and periodicity was assumed in all directions. The final size of the simulation box was then 9.466 × 9.184 × 12 nm. Covalent bonds were added to all Ti-O pairs within a 2 Å-cutoff. We used force field parameters for the TiO_2 slab from a recent parameterisation study [48]. The same force field was use to calculate the CG potential interactions between the surface and the 20 amino acids. The same folded Ubi structure as for the CG model was used and inserted above the TiO_2 slab. The TiO_2-Ubi system was solvated by insertion of 25,817 water molecules around the protein and the slab, and the final system contained 99,802 atoms. The system was energy minimized for 1000 steps and then equilibrated at constant temperature (300 K) and pressure (1 bar) for 100 ps using Berendsen's weak scaling algorithms [49], with relaxation constant τ = 1 ps in both cases. The temperature coupling was applied independently to the TiO_2 slab and to the rest of the system. The pressure tensor must be kept anisotropic due to the solid TiO_2 slab, but the off-diagonal components of the compressibility tensor (and the reference pressure tensor) were set to zero to enforce a rectangular simulation box. The diagonal elements of the compressibility tensor were set to 5×10^{-7} bar^{-1} in the lateral directions (bulk TiO_2) and 5×10^{-5} bar^{-1} in the normal direction (bulk water). The box vectors relaxed 2–4 % during equilibration.

In a first simulation, we placed the protein in the ($\phi = 0°$, $\theta = 0°$) orientation close to the surface and followed the dynamics for 440 ns at constant volume and 300 K. The Nose-Hoover thermostat [50, 51] with the coupling constant τ = 5 ps was used to ensure proper sampling of the ensemble when controlling the temperature. The simulation was run in parallel using 512 cores and frames were kept every 5 ps.

The trajectory obtained showed that the protein motion was diffusive in the bulk water for about 25 ns until making contact with the TiO_2 slab. Then the Ubi molecule attached to the surface and remained adsorbed for the rest of the simulation. To study the stability of the structure of the protein during adsorption we calculated the root-mean-square-deviation (RMSD) as a function of time and the results are shown in Fig. 7.9. The RMSD remained at a low constant value of ca. 0.2 nm^2 during the simulation, i.e. no unfolding occurred in the adsorbed state. This results clearly confirms that for the adsorption of Ubi on TiO_2 a rigid body model for the protein structure is well justified.

A detailed study of the simulation trajectory revealed that the protein motion could be characterized by four states, and that adsorption occurs through a two-step mechanism (Fig. 7.10). First, the protein diffuses freely in the bulk water. Second,

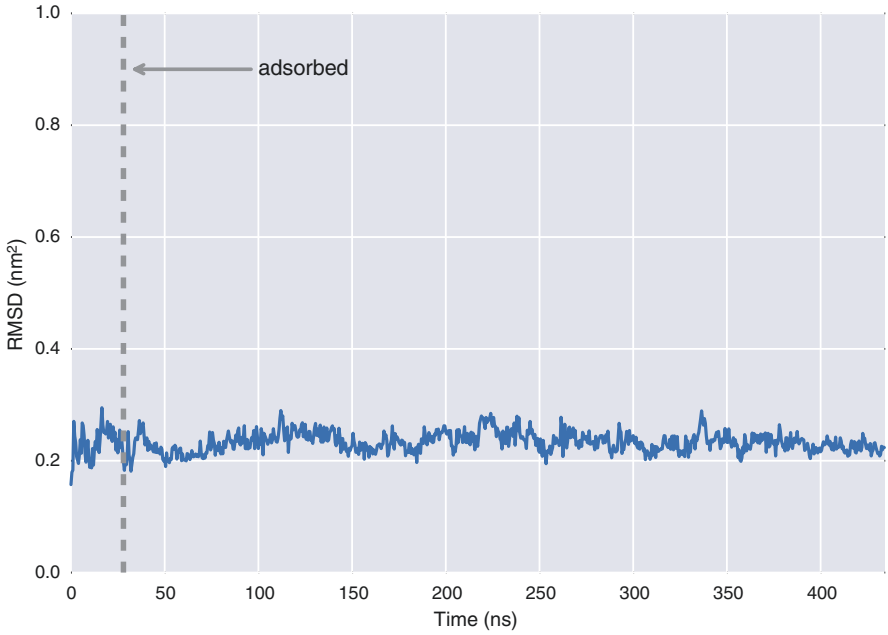

Fig. 7.9 The root-mean-square deviation (*RMSD*) of Ubi during the simulation with respect to the PDB reference structure. No unfolding occurs and the RMSD is 0.15 nm^2 throughout the simulation, which is the same as found in simulations of the folded structure in bulk water

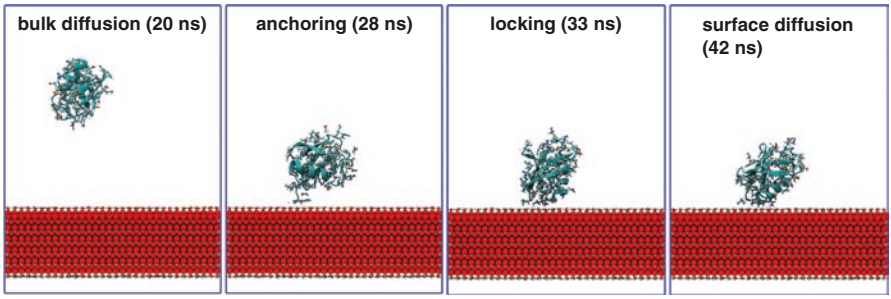

Fig. 7.10 Four distinct stages were identified during adsorption. (**a**) The protein diffuses in the bulk water. (**b**) The N-terminus of Ubi anchors to the solvation layer of the TiO_2 slab. (**c**) The protein rotates and locks to the solvation layer through GLN40 and GLN31. (**d**) The protein diffuses on the solvation layer in the locked conformation

the C-terminus of Ubi the protein contacts the TiO_2 surface and provides a lock for the protein to the first solvation layer. Third, Ubi rotates and locks into position on the surface. Fourth, the protein diffuses on the surface in the locked orientation.

The adsorption process is relatively fast once the first surface contact is initiated. The anchoring of the C-terminus to the first solvation layer occurs in about 5 ns and the locking is completed after 10 additional nanoseconds. The residues at the

C-terminus are ARG 74, GLY 75 and GLY 76. The anchoring is initiated when the charged end of ARG74 contacts the surface perpendicularly. The contact is not with the bare surface, but with the first solvation layer, which is strongly bound directly to the surface. At this point the rest of the protein diffuses in the bulk until (ca. 5 ns) GLU 40 can contact the surface, which leads to the protein being locked into an adsorbed orientation after 10 ns. The locking procedure consists of Ubi first connecting GLN40 to the surface, followed by a second connection through GLN31. The two glutamines (GLN31 and GLN40) form a bridge that stabilizes the orientation of the protein and no more changes in orientation occur for the rest of the simulation.

The residues involved in the anchor-lock mechanism are arginine and glutamine. These have been identified by potential of mean force calculations [48] of isolated side chain fragments (together with aromatic side chains) to be the strongest binders to TiO_2. In both cases, the NH_2-group of the end of the amino acid approaches the surface in a perpendicular orientation but can then rotate to maximize the interactions with the solvation layer.

The "upright" position of the protein in the adsorbed state suggests that it does not correspond to a free energy minimum. Since the orientation does not change over 400 ns, it is likely that there are high free energy barriers associated with the orientation changing into another free energy basin. To map all values of ϕ and θ, more sampling of the protein adsorption is needed. This could either be done in a repetitive fashion from different starting configurations or with enhanced sampling techniques such as metadynamics.

As for Ubiquitin we do not observe any unfolding within several hundreds of nanoseconds, we can conclude that our rigid protein model for studying adsorption is justified at least for some conditions: small NPs, non-metallic particles and small and compact proteins such that the adsorption energies are within few tens of k_BT. For other situations, one should evaluate the energy to decide whether the model is sufficient. In general, conformational changes can be an important factor for the adsorption dynamics process [44]. This assumption can be relaxed by e.g. using a Gō–Type model (see [34] for a review on CG models of proteins). Furthermore, as the methodology we presented is computationally very efficient and can provide information about the structure of NP-protein complexes, it can be used as an exploring tool to perform more sophisticated and computationally demanding calculations.

7.3 Coarse-Grained Model of a Lipid Bilayer

Any attempt to simulate with some molecular details but at length and time scale involve in the uptake of NPs through a cell membrane must rely on a CG model of the main constituents of the biological membranes. In this section we describe a methodology to systematically CG a lipid bilayer and lipid bilayer containing Cholesterol from the results of full atomistic simulations.

Table 7.3 Composition of the simulations used for the CG of lipids mixtures

System	I. DMPC-Cholesterol	II. DMPC-DOPS	III. DOPS-Cholesterol
Number of DMPC	30	30	–
Number of DPPS	–	30	30
Number of Cholesterol	30	–	30
Number of water	2000	2000	2000
Number of Na+	–	30	30

7.3.1 Molecular Simulations of Various Lipid-Cholesterol Mixtures

We started the CG procedure by performing all-atom molecular dynamics simulations for three lipid mixtures: (i) 1,2-dimyristoyl-sn-glycero-3-phosphatidylcholine with Cholesterol (DMPC + CHOL); (ii) 1,2-dioleoyl-sn-glycero-3-phosphatidylserine with Cholesterol (DOPS + CHOL); (iii) 1,2-dimyristoyl-sn-glycero-3-phosphatidylcholine with 1,2-dioleoyl-sn-glycero-3-phosphatidylserine (DMPC + DOPS). The composition of this systems are reported in the Table 7.3. In each simulation, the starting state was generated randomly and energy was minimized afterwards. Then a short 1 ns NVT simulation at density 1 g/cm^3 was carried out, which was followed by a 100 ns equilibration simulation in NPT-ensemble and a production stage of 400 ns. The Slipids force field was used [52, 53]. Other simulation parameters: time step 2 fs; Nose-Hoover isotropic thermo/barostat with temperature 303 K, pressure 1 bar, relaxation times 0.1 and 1 ps for thermostat and barostat respectively; all bonds were constrained by Links algorithm; particle-mesh Ewald with Fourier spacing 1 Å and tolerance parameter 10^{-5}. The configurations were saved in the trajectory each 10 ps. The atomistic simulations were performed using the Gromacs simulation engine (v. 4.5) and a rigid TIP3P water model.

7.3.2 Mapping of Atomistic to Coarse-Grained Trajectories: From Residue to Beads

The atomistic trajectories obtained in the simulations were mapped onto CG trajectories, and radial distribution functions between sites of the CG models have been determined. As shown in Fig. 7.11, 10 beads for representation of DMPC molecule were used at the CG level (3 beads instead of each of the two hydrocarbon tails, 4 beads instead of the head group including esters), 14 beads for DOPS molecule (5 beads instead of each hydrocarbon tail with specific distinguishing of the beads with double bond and beads uniting 3 or 4 methylene groups, and 4 beads instead of the head group), 5 beads for CHOL molecule, and Na+ ions as a single bead were used. Water was not included into CG model but its effect was included into

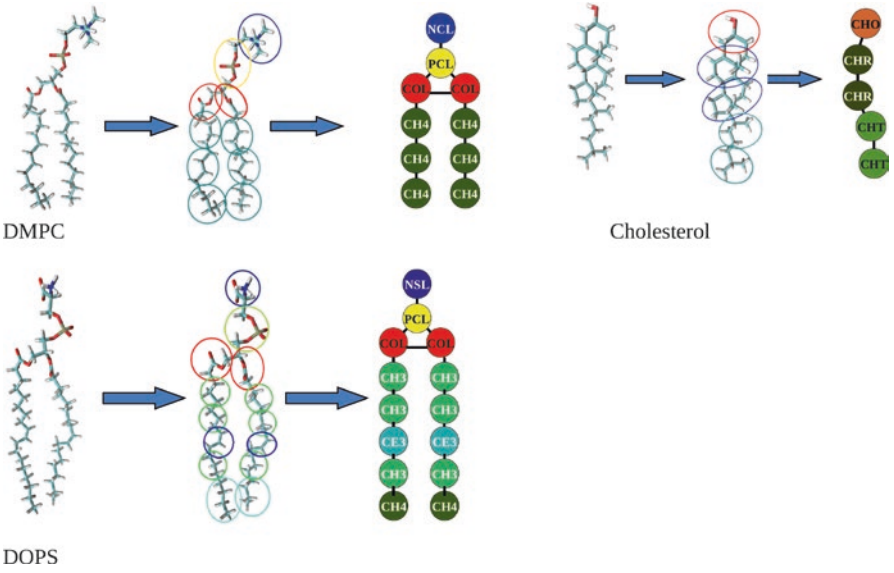

Fig. 7.11 Mapping of systems at an atomistic level to a CG level where each residue of the atomistic system is replaced by a bead for DMPC, Cholesterol and DOPS (1,2-dioleoyl-sn-glycero-3-phosphatidylserin) molecules. CG sites of the same type are given by the same color

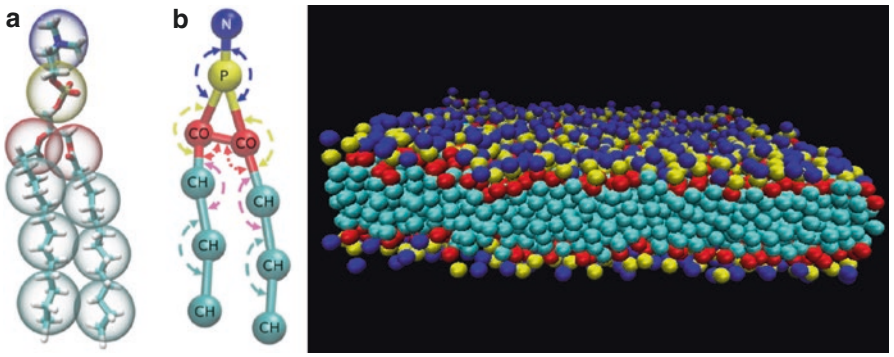

Fig. 7.12 Simulation snapshot of a single CG DMPC lipid molecule (*left*) and of self-assembled DMPC bilayer 15 × 15 nm containing 762 lipids (*right*)

solvent-mediated potentials. Figure 7.12 shows a snapshot of CG DMPC bilayer, which is spontaneously formed in a CG lipid system.

The radial distribution functions (RDF) between CG sites obtained after coarse-graining of the atomistic trajectories were used to compute effective potentials defining interactions in the CG models using the inverse Monte Carlo method. The RDF were computed for each pair of different CG sites and were used as an input to compute effective CG potentials which reproduce the RDFs. Computations of effective potentials were done for the same compositions of the systems I, II, and III as

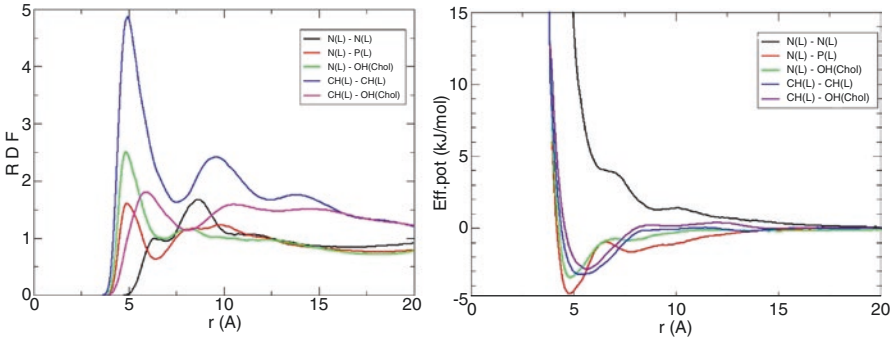

Fig. 7.13 Extraction via Inverse Monte Carlo of CG site-site pair potentials from atomistic RDF's. Five site-site RDFs (*left*) and corresponding effective potentials involving DMPC CG sites of total 28 for DMPC-CHOL mixture (*right*) are shown

the respective atomistic simulations listed in Table 7.3. The software package MagiC [54] was used. In the inversion process, the first 20 iterations have been carried out using iterative Boltzmann inversion, followed by 30–40 iterations using the inverse Monte Carlo algorithm.

More specifically, the RDF's have been determined between beads involved in "non-bonded" interactions, that is between CG sites belonging different molecules or the same molecule but separated by more than two bonds. Also, reference distribution functions for the bond lengths and bending angle distribution functions were determined for the all CG sites relevant for the three types of considered molecules. Then the calculated RDFs and bonded reference distribution functions were used to calculate parameters of the corresponding CG potentials. This is a multistage process, from a high resolution system description to a low resolution one. Monte Carlo computer simulations of the CG system DMPC + CHOL using Metropolis method (MagiC package) were carried out. The parameters were calculated using a two-step iteration technique: first, the iterative Boltzmann inversion method was performed to calculate a set of intermediate parameters; second, the inverse Monte Carlo algorithm was used to calculate the final set of parameters. The final parameters of the CG potentials for DMPC + CHOL mixture have been calculated (see Fig. 7.13).

7.3.3 Validation of the Lipid Coarse-Grained Model

The interaction potentials obtained for the CG models using the inverse Monte Carlo technique were validated by comparison with atomistic simulations. Figure 7.14 shows radial distribution functions between some selected sites of DMPC lipid and Cholesterol computed in CG and atomistic simulations of a mixture of 30 DMPC lipids, 30 Cholesterol molecules and 1800 waters. The result shows a perfect

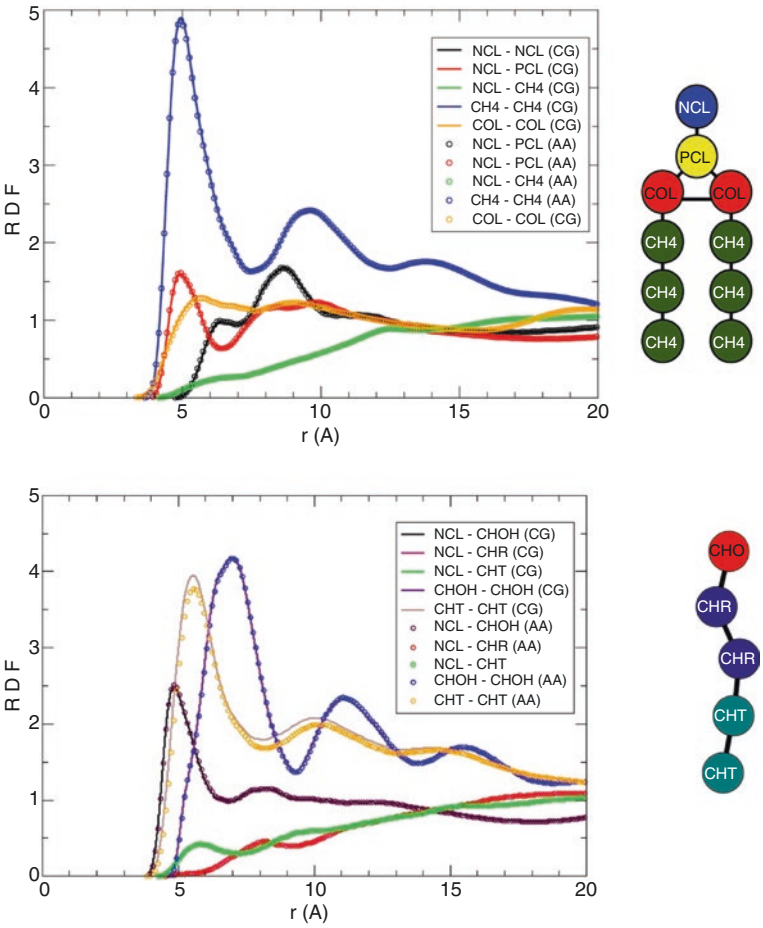

Fig. 7.14 RDFs between different sites of DMPC (*top graph*) and Cholesterol (*bottom graph*) molecules, see site definitions to the right of the graph. Atomistic (*points*) and CG (*lines*) simulations were carried out for a mixture of 30 DMPC, 30 Cholesterol, and 1800 water molecules (CG simulation were without explicit water but in a box of the same size as atomistic simulations including water)

coincidence of the RDFs, which justifies the approximations made and the quality of the CG model.

Figure 7.12 shows a snapshot of CG DMPC bilayer, which is spontaneously formed in a CG lipid system. We have carried out a number of simulations of flat lipid bilayers composed of CG lipid models representing other lipids which can be built from the CG sites presented in Fig. 7.11. These simulations were carried out at zero-tension conditions within the atomistic and CG models. Table 7.4 shows comparison of some properties not related to the RDFs obtained within atomistic and CG simulations of a piece of bilayer composed of 128 DMPC lipids. Very good agreement is observed for the average area per lipid (which is one of the most

Table 7.4 Comparison of the properties of the DMPC bilayer obtained from the full atomistic simulations and the CG model

	Area per lipid	Compressibility	Tail order parameters	
	(Å)	(10^{14} N/nm)	(1)	(2)
Atomistic	60	1.9	0.57	0.52
CG	59	2.5	0.56	0.52

Table 7.5 Average areas per lipid. Comparison of simulation results computed in CG simulations and experiments at T = 303 K

	Area per lipid (Å^2)	
Lipid	Sim	Exp
DMPC (14:0/14:0 PC)	59.0	60.5 [56]
SOPC (18:0/18:1n9 PC)	60.4	61.1 [57]
DOPC (18:1n9/18:1n9 PC)	62.0	67.4 [58]
DSPC (18:0/18:0)	43.5[a]	44.5[a,b] [55]

[a]Bilayer in gel phase
[b]Evaluated in atomistic MD simulations

important parameters for a lipid bilayer) and for the tail order parameter, and a reasonably good agreement for the bilayer compressibility. Especially important is the agreement for the order parameter, which shows that orientational fluctuations of the lipid tails are the same in atomistic and CG models.

Table 7.5 shows average areas per lipid obtained in CG simulations carried out in conditions of zero tension and experiment for a number of lipids. Except DMPC, other lipids included in this table were not used in the parameterization of the CG potentials. The models for these lipids were built from appropriate sites of DMPC and DOPS lipids shown in Fig. 7.11, and the CG interaction potentials were taken as determined in IMC computations for DMPC and DOPS lipids (some of them shown in Fig. 7.13). One can see generally good agreement with experiment, though simulations show a tendency for some underestimation of the lipid area. The bilayer composed of DSPC lipids was found in the gel phase which again is in agreement with experiment (the temperature of gel phase transition for DSPC is 55 °C). We are not aware on an experimental value of the average lipid area for the gel phase of DSPC, but it is generally accepted that average area per lipid in the gel phase is in the range 43–48 Å^2 for phosphatidylcholine lipids. Also, atomistic simulations of DSPC bilayer in a gel phase [55] reports the average lipid area of 44.5 Å^2, which is in good agreement with the result of our CG model.

7.4 NP and Bilayer Simulation

Using the methodologies described in Sects. 7.2 and 7.3, we now can construct a model to simulate the interaction of a DPMC lipid bilayer with a small hydrophobic NP and a hydrophobic NP associated with one molecule of HSA. Following is the description of the simulations and the main results.

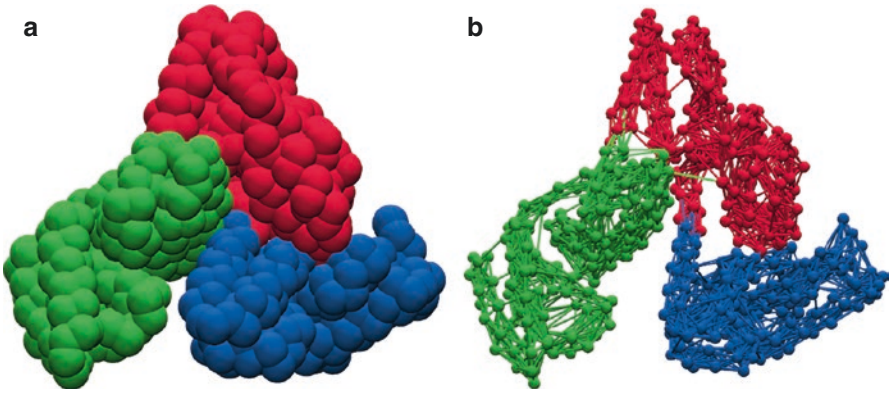

Fig. 7.15 (**a**) CG model of HSA protein used in this study. Each residue is represented by a single bead located at the position of the α-carbon. Each color represents one of the three domains of the HSA molecule. (**b**) All beads separated by less than 10 nm are connected by stiff harmonic bonds

7.4.1 Interaction Potentials and Parameters of the Simulations

The simulated systems are composed of the NP, the lipids that form the bilayer, the amino acids of the HSA, and monovalent ions that are used to resemble physiological conditions. For all interactions we assume two contributions: electrostatic and van der Waals interactions. For the electrostatic contribution, all charged beads interact through a Coulomb potential between given by:

$$U^{C}\left(r_{ij}\right) = \lambda_{B} k_{B} T \frac{q_i q_j}{r_{ij}} \tag{7.9}$$

where r_{ij} is the distance between the bead i and the bead j, λ_B is the Bjerrum length and q_i and q_j are the charges of the beads i and j respectively. The calculation of this long-range interaction was implemented through an Ewald summation P3M algorithm [42]. The Bjerrum length is set to 0.71 nm in all cases. Note that in the MD simulation, the background salt ions are explicitly present, so we do not need to employ the screened Coulomb potential Eq. (7.5).

For the van der Waals interactions we use the following model:

- Aminoacid – aminoacid van der Waals interactions: we do not explicitly consider interaction between any pair of aminoacids within the single protein molecule as the protein is not allowed to change conformation from the PDB crystal structure. To improve the computational efficiency instead of simulating the HSA molecule as a rigid body, we connect all residues which are separated less than 10 nm by harmonics bonds with a spring constant of $100 k_B T$. Figure 7.15a shows the resulting CG model for the HSA (build according to PDB ID:1N5U), while Fig. 7.15b shows the resulting network of bonds (8059 in total).

- NP – aminoacid van der Waals interactions: we used the interaction potential defined in Eq. (7.2) and the same parameters for the aminoacids and the NP obtained by the parameterization described in Sect. 7.2.3.
- Lipid-lipid interactions: the CG models of the lipids in the bilayer and the interactions between the four different types of beads were obtained as described in Sect. 7.3**.**
- Lipid-NP interactions: we used the same interaction potentials as in the case of NP-aminoacid interaction Eq. (7.2) and assumed that lipid beads interact with the surface according to their hydrophobicity. We classify the lipid beads into one of two groups: head or tail. The head beads are NCL, PCL and COL (see Fig. 7.11), and they are considered to be hydrophilic with a value of $\varepsilon_i = 0.1$. The tail beads (labeled CH4 in Fig. 7.11) are hydrophobic and a value of $\varepsilon_i = 0.75$ is used for these groups. The van der Walls radius of all the lipids beads is set to σ_i = 0.6 nm.
- Lipid-aminoacid interactions: for these interactions we use the same approach as for the NP-residues and NP-lipid. The potential interaction is also based on the hydrophobicity of the beads given by the following modified 12-6 Lennard-Jones potential:

$$U_{l,i}(r) = \begin{cases} 4\varepsilon_{la}\left[\left(\dfrac{\sigma_{l,i}}{r}\right)^{12} - \left(\dfrac{\sigma_{l,i}}{r}\right)^{6}\right] + \varepsilon_{la}\left(1-\varepsilon_{l,i}\right) & r < r_c \\ 4\varepsilon_{la}\,\varepsilon_{l,i}\left[\left(\dfrac{\sigma_{l,i}}{r}\right)^{12} - \left(\dfrac{\sigma_{l,i}}{r}\right)^{6}\right] & r_c \le r \le r_{\text{cut}} \\ 0 & r > r_{\text{cut}} \end{cases} \tag{7.10}$$

where r is the distance from the lipid bead l to the residue i, ε_{la} is a free parameter that scales the interaction energy, $\varepsilon_{l,i}$ is the combined hydrophobicity index of lipid l and the residue i and is given by $\varepsilon_{i,s} = \sqrt{\varepsilon_i\,\varepsilon_s}$, $\sigma_{s,i}$ is the average van der Waals radius of residue i and the lipid l, $\sigma_{l,i} = (\sigma_l + \sigma_i)/2$, $r_c = 2^{1/6}\sigma_{l,i}$ and r_{cut} is the cut-off for the van der Waals interaction. As in this work we only study the applicability of the proposed methodology we do not systematically parameterize the value of ε_{la}, instead we set this scaling parameter to $0.5k_BT$ for all simulations. This values gives interactions between the lipids and the residues in the same order of magnitude as the ones reported in [59].
- Ion-ion and ion-molecule interactions: in addition to the Coulomb forces, we include excluded volume interactions by means of a WCA potential. The van der Waals radii of the ions are set to 0.2 nm.

For all simulations a NP of radius 2 nm is used with a surface charge of -0.02 C/m^2. We use NVT ensemble with the box size was 15 × 15 × 20 nm and we assume physi-

ological conditions with monovalent salt concentration of 0.1 M (270 negative and positive ions are placed in the simulation box). For a larger NP, NPT simulation would be necessary. To keep charge neutrality, further 16 positive ions are added. The bilayer is composed of a total of 762 lipids (381 lipids in each layer). A Langevin thermostat with a friction coefficient of γ=0.05 is used and the units of mass, energy and charge are the same as described in Sect. 7.2.3. The time unit (τ) is obtained by performing a simulation of the bilayer with ions (no NP or proteins are added) and measuring the lateral diffusion constant. We obtained a value of 8×10^{-5} nm^2/τ, which compared with the experimental value of 5 μm^2/s gives τ = 16 ps.

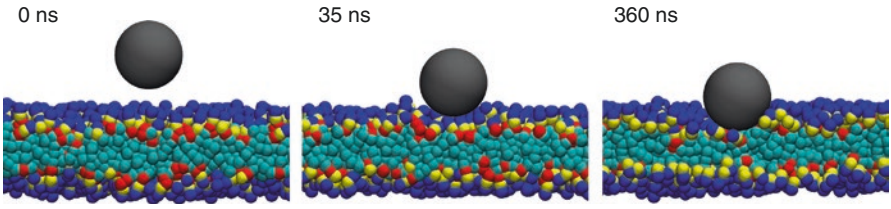

Fig. 7.16 Time sequence of simulation snapshots illustrating the interaction of a DMPC lipid bilayer with a negatively charged hydrophobic NP. The radius of the NP is 2 nm. The ions are not shown

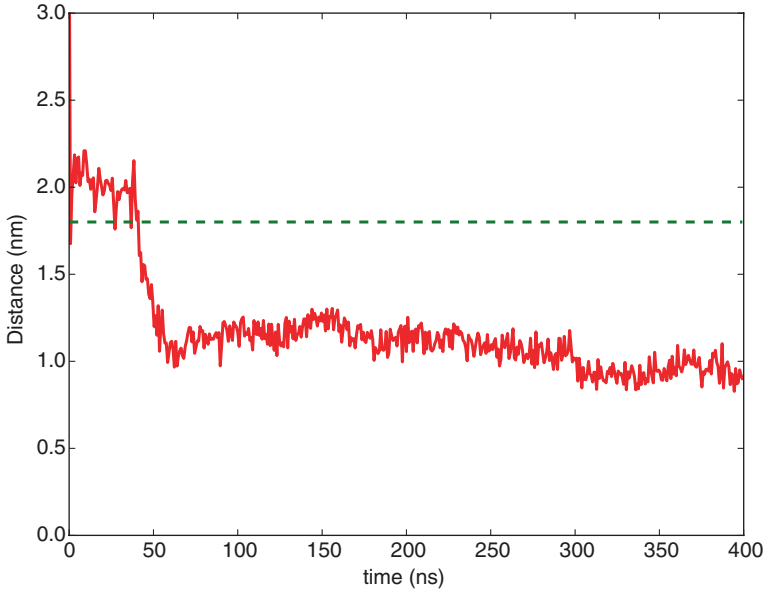

Fig. 7.17 Distance of the surface of the bare NP to the center of the bilayer as a function of time. The dashed line shows the average position of the bilayer surface

7.4.2 Simulation of a Nanoparticle in Contact with a Lipid Bilayer

To study the interaction of a bare NP with the lipid bilayer we initially position the NP close to the bilayer surface and follow the time dynamics of the system. Three snapshots are shown Fig. 7.16. From the initial state the NP adsorbs quickly to the surface of the bilayer and then penetrates to around 1 nm inside the membrane and stays strongly attached until the end of the simulation (see snapshots at 35 and 360 ns). To explore the adsorption process in more detail, the distance of the surface of the NP to the center of the bilayer was recorded and the results are shown in Fig. 7.17. The NP reaches the bilayer in a few nanoseconds and then attaches to the surface for around 50 ns (the dashed line in Fig. 7.17 marks the average position of the surface of the lipid bilayer, as defined by the position of the maximum of density of the lipid headgroups). After that, the NP starts penetrating the membrane (in a few nanoseconds). Then a slow internalization is observed until the NP reaches its final position at approximately 300 ns. The internalization of the NP is mediated by the attractions between both type of lipids and the NP. The penetration then stops (or becomes much slower) because any further displacement requires a substantial change in the membrane structure. To study long-time dynamics of the system, NP lipid wrapping and uptake one needs a bigger bilayer or/and NPT ensemble [60]. Despite of this limitation, the results obtained with our methodology agree with a recent report [61] for the absorption of a hydrophobic NP with a membrane composed of lipids and specialized receptors.

7.4.3 Simulation of a Nanoparticle-Protein Complex in Contact with a Lipid Bilayer

As we discussed above, the NP gets coated by proteins before it reaches the cell membrane, and this NP-protein complex is responsible for the final fate of the NP [62]. Considering this, we now simulate the interaction of a NP-protein complex, where protein corona is represented by a single HSA molecule. As shown in Sect. 7.2, not all orientations in which protein adsorbs onto a surface are equally probable and for our simulation of the interaction of a hydrophobic NP with a DPMC lipid membrane we first calculate the adsorption energy map of HSA onto a 2 nm of radius hydrophobic NP. The adsorption map is shown in Fig. 7.18a. We can see that, as in the cases discussed above, the energy landscape contains more than one minimum. We found the average adsorption energy of $-1.7k_BT$ and as the initial orientation for the simulation we selected the orientation $(\theta, \phi) = (145°, 110°)$, which corresponds to adsorption energy of $-2.7k_BT$ and the corresponding complex NP-HSA is shown in Fig. 7.18b.

Figure 7.19 shows a sequence of snapshots from simulation of the NP-HSA complex with the lipid bilayer. In the initial state, the protein is facing the bilayer. In the

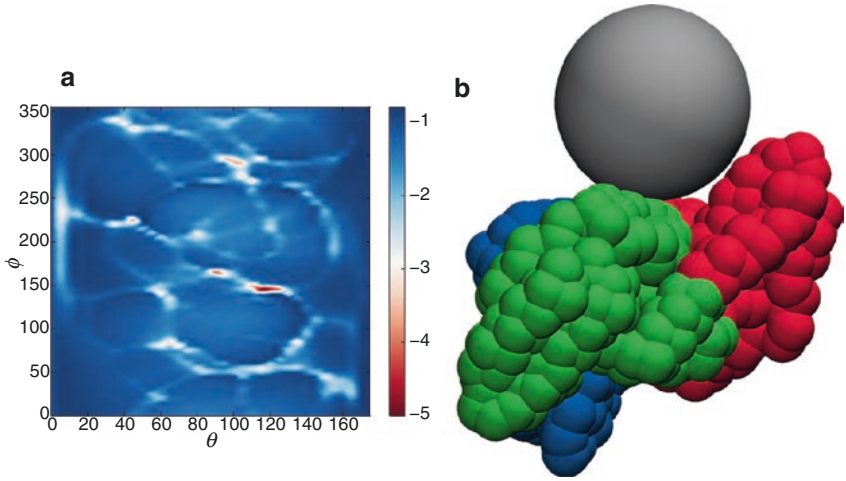

Fig. 7.18 (**a**) Initial state of the NP-HSA complex. (**b**) Surface map of the adsorption orientations of HSA onto a 2 nm negatively charged hydrophobic NP

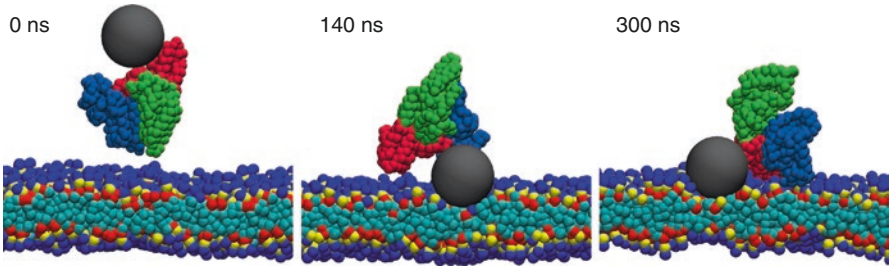

Fig. 7.19 Time sequence of the snapshots of the interaction of a DMPC lipid bilayer with a negatively charged hydrophobic NP complex with one HSA molecule. The radius of the NP is 2 nm. The ions are not shown

simulation, the HSA at first moves in front of the membrane and prevents a direct contact between the NP and the lipids. Then, the NP-HSA complex rotates so that the NP faces the bilayer and starts penetrating the membrane. Figure 7.20 shows the distance of the NP surface to the center of the membrane. The rotation is reflected in the sudden change of the position of COM of the HSA. After this quick rearrangement the NP starts the penetration while the protein stays attached to the NP for the whole simulation but moves around the surface of the NP as can be seen in the snapshot for the times 140 and 300 ns in Fig. 7.19. This movement of the HSA molecule can also be observed from the curve of the COM of the HSA curves as a function of time (Fig. 7.20).

Comparing the two simulations we see that the presence of the HSA dramatically changes the interaction of the NP with the membrane. We can envision that a NP,

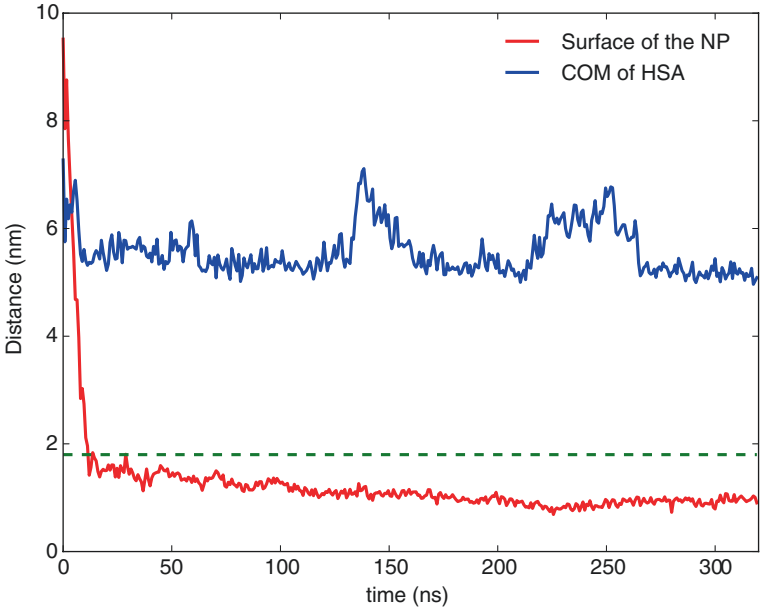

Fig. 7.20 Distance of the surface of the complex of NP with one HSA to the center of the bilayer and the COM of the HSA as a function of time. The dashed line shows the average position of the bilayer surface

fully coated NP with HSA, will not be able to penetrate into the membrane, so the coating is changing completely its biological reactivity.

7.5 Conclusions

In this work, we presented a multiscale methodology for modelling interactions at bionano interface, which is central for understanding uptake and toxicity of nanomaterials. We used systematic coarse-graining techniques to reduce the complexity of the problem by removing some degrees of freedom and focussing on the properties of interest. Since the CG models consists of about ten times less interaction centres than the atomistic model, and the solvent (water) is not modeled explicitly, simulations of the CG model take two to three orders of magnitude less CPU time compared with atomistic simulations for equal system size, or, alternatively, CG model can be used for simulations of whole proteins, small NPs and sufficiently large cell membrane fragments at the scale of tens of nanometers. We have parameterised and validated the model against experiments and all-atom MD simulations.

The technique for coarse-graining NP-protein interaction, which we presented in Sect. 7.2 can be used to calculate the binding energies for arbitrary plasma,

cytosol, or membrane proteins, rank them by binding affinity to the NP and predict the content of NP protein corona. Our calculations show that the NP surface charge has a small effect on the adsorption energies in comparison to van der Waals interactions between the residues and the surface. We also find that the charge of the NP does not influence much the orientation, in which the protein prefers to adsorb. On the other hand, we have shown the size of the NP has a big effect on the adsorption energy maps, due to the amount of material involved and because the curvature of the NP determine the sections of the protein that can interact with the surface. Based on our simulations results, we can predict bigger proteins adsorb stronger on the inorganic surfaces, even for small NPs, in agreement with the Vroman effect. We have also demonstrated that a rigid protein model is justified at least for small globular proteins. In Sect. 7.3, we have parameterised a CG lipid and Cholesterol model, which reproduces the key bilayer properties of atomistic model of the same system. Finally, in Sect. 7.4, we have shown how the CG lipid and NP-protein models can be combined to model NP-cell membrane interactions and NP attachment and uptake.

References

1. Sharifi S, Behzadi S, Laurent S, Forrest ML, Stroevee P, Mahmoudi M (2012) Toxicity of nanomaterials. Chem Soc Rev 41:2323
2. Borm PJA et al (2006) The potential risks of nanomaterials. Part Fibre Toxicol 3:11
3. Johnston HJ, Hutchison GR, Christensen FM et al (2009) Identification of the mechanisms that drive the toxicity of tio2 particulates: the contribution of physicochemical characteristics. Part Fibre Toxicol 6:33
4. Nel AE, Maedler L, Velegol D et al (2009) Understanding biophysicochemical interactions at the nano-bio interface. Nat Mater 8:543
5. Verma A, Uzun O, Hu Y et al (2008) Surface-structure-regulated cell-membrane penetration by monolayer-protected nanoparticles. Nat Mater 7:588
6. Schlick T, Collepardo-Guevara R, Halvorsen LA et al (2011) Biomolecular modeling and simulation: a field coming of age. Q Rev Biol 44:191
7. Valerio LG Jr (2009) In silico toxicology for the pharmaceutical sciences. Toxicol Appl Pharmacol 241:356
8. Nigsch F, Macaluso NJ, Mitchell JB, Zmuidinavicius D (2009) Computational toxicology: an overview of the sources of data and of modelling methods. Expert Opin Drug Metab Toxicol 5:1
9. Dearden JC (2003) In silico prediction of drug toxicity. J Comput Aided Mol Des 17:119
10. Lyubartsev AP, Rabinovich AL (2011) Recent development in computer simulations of lipid bilayers. Soft Matter 7:25
11. Wong-Ekkabut J, Baoukina S, Triampo W, Tang I-M, Tieleman DP (2008) Computer simulation study of fullerene translocation through lipid membranes. Nat Nanotechnol 3:363
12. Hou WC, Moghadam BY, Westerhoff P, Posner JD (2011) Distribution of fullerene nanomaterials between water and model biological membranes. Langmuir 27:11899
13. Yang K, Ma YQ (2010) Computer simulation of the translocation of nanoparticles with different shapes across a lipid bilayer. Nat Nanotechnol 5:579
14. Monticelli L, Salonen E, Ke PC, Vattulainen I (2009) Effects of carbon nanoparticles on lipid membranes: a molecular simulation perspective. Soft Matter 5:4433

15. Izvekov S, Voth GA (2005) Multiscale coarse-graining method for biomolecular systems. J Phys Chem B 109:2469
16. Ayton GS, Noid WG, Voth GA (2007) Multiscale modeling of biomolecular systems: in serial and in parallel. Curr Opin Struct Biol 17:192
17. Lyubartsev AP, Laaksonen A (1995) Calculation of effective interaction potentials from radial distribution functions: a reverse monte carlo approach. Phys Rev E 52:3730
18. Lyubartsev AP, Mirzoev A, Chen L-J, Laaksonen A (2010) Systematic coarse-graining of molecular models by the newton inversion method. Faraday Discuss 144:43
19. Lyubartsev AP, Laaksonen A (1999) Effective potentials for ion-DNA interactions. J Chem Phys 111:11207
20. Tozzini V (2005) Coarse-grained models for proteins. Curr Opin Struct Biol 15(2):144–150
21. Bereau T, Deserno M (2009) Generic coarse-grained model for protein folding and aggregation. J Chem Phys 130(23):235106
22. Takada S (2012) Coarse-grained molecular simulations of large biomolecules. Curr Opin Struct Biol 22(2):130–137
23. Wei S, Knotts T (2013) A coarse grain model for protein-surface interactions. J Chem Phys 139(9):095102
24. Lobaskin V, Lyubartsev AP, Linse P (2001) Effective macroion-macroion potentials in asymmetric electrolytes. Phys Rev E 63:020401
25. Brunner M, Bechinger C, Strepp W, Lobaskin V, von Gruenberg HH (2002) Density-dependent pair interactions in 2D colloidal dispersions. Europhys Lett 58:926
26. Lynch I, Salvati A, Dawson KA (2009) Protein-nanoparticle interactions. What does the cell see? Nat Nanotechnol 4:546
27. Lynch I, Dawson KA, Linse S (2006) Detecting cryptic epitopes created by nanoparticles. Sci STKE 2006:14
28. Cedervall T et al (2007) Understanding the nanoparticle protein corona using methods to quantify exchange rates and affinities of proteins for nanoparticles. Proc Natl Acad Sci U S A 104:2050
29. Lindman S et al (2007) Systematic investigation of the thermodynamics of HSA adsorption to n-iso-propylacrylamide/n-tert-butylacrylamide copolymer nanoparticles. effects of particle size and hydrophobicity. Nanoletters 7:914
30. Allen LT et al (2006) Surface-induced changes in protein adsorption and implications for cellular phenotypic responses to surface interaction. Biomaterials 27:3096
31. Radke CE, Prausnitz JM (1972) Thermodynamics of multisolute adsorption from dilute liquid solutions. AIChE J 18:761
32. Lesniak A, Campbell A, Monopoli MP, Lynch I, Salvati A, Dawson KA (2010) Serum heat inactivation affects protein corona composition and nanoparticle uptake. Biomaterials 31:9511
33. Kamath P, Fernandez A, Giralt F, Rallo R (2015) Predicting cell association of surface-modified nanoparticles using protein corona structure – activity relationships (PCSAR). Curr Top Med Chem 15(18):1930–1937
34. Noid WG (2013) Perspective: Coarse-grained models for biomolecular systems. J Chem Phys 139(9):090901
35. Lopez H, Lobaskin V (2015) Coarse-grained model of adsorption of blood plasma proteins onto nanoparticles. J Chem Phys 143:243138
36. Miyazawa S, Jernigan RL (1996) Residue-residue potentials with a favorable contact pair term and an unfavorable high packing density term, for simulation and threading. J Mol Biol 256(3):623–644
37. Kim Y, Tang C, Clore G, Hummer G (2008) Replica exchange simulations of transient encounter complexes in protein-protein association. Proc Natl Acad Sci U S A 105(35): 12855–12860
38. Kim Y, Hummer G (2008) Coarse-grained models for simulations of multiprotein complexes: application to ubiquitin binding. J Mol Biol 375(5):1416–1433
39. Agashe M, Raut V, Stuart S, Latour R (2005) Molecular simulation to characterize the adsorption behavior of a Fibrinogen γ-chain fragment. Langmuir 21(3):1103–1117

40. Sun Y, Welsh W, Latour R (2005) Prediction of the orientations of adsorbed protein using an empirical energy function with implicit solvation. Langmuir 21(12):5616–5626
41. Kokh D, Corni S, Winn P, Hoefling M, Gottschalk K, Wade R (2010) Prometcs: An atomistic force field for modeling proteinmetal surface interactions in a continuum aqueous solvent. J Chem Theory Comput 6(5):1753–1768
42. Limbach H, Arnold A, Mann B, Holm C (2006) ESPResSo – an extensible simulation package for research on soft matter systems. Comput Phys Commun 174(9):704–727
43. Chen W, Huang H, Lin C, Lin F, Chan Y (2003) Effect of temperature on hydrophobic interaction between proteins and hydrophobic adsorbents: studies by isothermal titration calorimetry and the van't Hoff equation. Langmuir 19(22):9395–9403
44. Lacerda S, Park JJ, Meuse C, Pristinski D, Becker M, Karim A, Douglas J (2010) Interaction of gold nanoparticles with common human blood proteins. ACS Nano 4(1):365–379
45. Vilaseca P, Dawson K, Franzese G (2013) Understanding and modulating the competitive surface-adsorption of proteins through coarse-grained molecular dynamics simulations. Soft Matter 9:6978–6985
46. Vijay-Kumar S, Bugg C, Cook W (1987) Structure of ubiquitin refined at 1.8 resolution. J Mol Biol 194:531–544
47. Momma K, Izumi F (2011) *VESTA3* for three-dimensional visualization of crystal, volumetric and morphology data. J Appl Cryst 44:1272–1276
48. Brandt EG, Lyubartsev A (2015) Systematic optimization of a force field for classical simulations of TiO_2-water interfaces. J Phys Chem C 119:18110–18125
49. Berendsen HJC, Postma JPM, van Gunsteren WF, DiNola A, Haak JR (1984) Molecular dynamics with coupling to an external bath. J Chem Phys 81:3684–3690
50. Hoover W (1985) Canonical dynamics: equilibrium phase-space distributions. Phys Rev A 31:1695–1697
51. Nose S (1984) A unified formulation of the constant temperature molecular dynamics methods. J Chem Phys 81:511–519
52. Jämbeck JPM, Lyubartsev AP (2012) Derivation and systematic validation of a refined all-atom force field for phosphatidylcholine lipids. J Phys Chem B 116(10):3164–3179
53. Jämbeck JPM, Lyubartsev AP (2013) Another piece of the membrane puzzle: extending Slipids further. J Chem Theory Comput 9(1):774–784
54. Mirzoev A, Lyubartsev AP (2013) MagiC: software package for multiscale modeling. J Chem Theory Comput 9(3):1512–1520
55. Qin S-S, Yu ZW, Yu Y-X (2009) Structural characterization on the gel to liquid-crystal phase transition of fully hydrated DSPC and DSPE bilayers. J Phys Chem B 113:8114–8123
56. Kučerka N, Liu Y, Chu N, Petrache HI, Tristram-Nagle S, Nagle JF (2005) Structure of fully hydrated fluid phase DMPC and DLPC lipid bilayers using X-ray scattering from oriented multilamellar arrays and from unilamellar vesicles. Biophys J 88:2626–2637
57. Koenig BW, Strey HH, Gawrisch K (1997) Membrane lateral compressibility determined by NMR and X-ray diffraction: effect of acyl chain polyunsaturation. Biophys J 73(4): 1954–1966
58. Kučerka N, Nagle JF, Sachs JN, Feller SE, Pencer J, Jackson A, Katsaras J (2008) Lipid bilayer structure determined by the simultaneous analysis of neutron and X-Ray scattering data. Biophys J 95(5):2356–2367
59. Bereau T, Wang Z-J, Deserno M (2014) More than the sum of its parts: Coarse-grained peptide-lipid interactions from a simple cross-parametrization. J Chem Phys 140(11):115101
60. Lin J, Zhang H, Chen Z, Zheng Y (2010) Penetration of lipid membranes by gold nanoparticles: Insights into cellular uptake, cytotoxicity, and their relationship. ACS Nano 4(9):5421–5429
61. Hong-Ming D, Yu-Qiang M (2014) Computer simulation of the role of protein corona in cellular delivery of nanoparticles. Biomaterials 35(30):8703–8710
62. Monopoli M, Aberg C, Salvati A, Dawson KA (2012) Biomolecular coronas provide the biological identity of nanosized materials. Nat Nanotechnol 7(12):779–786